

## Innovative in-flight glass-melting technology using thermal plasmas\*

Takayuki Watanabe<sup>1,‡</sup>, Kazuyuki Yatsuda<sup>1</sup>, Yaochun Yao<sup>1</sup>,  
Tetsuji Yano<sup>2</sup>, and Tsugio Matuura<sup>3</sup>

<sup>1</sup>*Department of Environmental Chemistry and Engineering, Tokyo Institute of Technology, Yokohama, 226-8502, Japan;* <sup>2</sup>*Department of Chemistry and Materials Science, Tokyo Institute of Technology, Tokyo, 152-8550, Japan;* <sup>3</sup>*Industrial Technology Center of Fukui Prefecture, Fukui, 910-0102, Japan*

**Abstract:** A stable 12-phase AC arc was generated by transformers at a commercial electric power system, and the arc behavior was characterized by image analysis. For the unique advantages, the multiphase AC arc was developed to apply to in-flight glass melting for the purpose of energy-saving and emission reduction. The effects of electrode configuration and sheath gas flow rate on the arc and melting behavior of granulated glass raw material were investigated. Results show that the discharge behavior and the high-temperature region can be controlled by the electrode configuration. The luminance area of the high-temperature region and its fluctuation reflect the discharge behavior. The vitrification degree of glass raw material is mostly dependent on the center temperature of arc. As sheath gas flow rate increases, the ratio of luminance area decreases and the center temperature of arc increases.

**Keywords:** arc discharge; glass production; in-flight melting; multiphase AC arc; thermal plasma.

### INTRODUCTION

The glass industry is a large global industry that annually produces more than 100 million tons of glass products such as sheet glass, container glass, fiber glass, and optical glass. Most glass has been produced by typical Siemens-type melter fired in air with heavy oil or natural gas as the fuel. This type of melter has been used for more than 140 years because of its good large-scale performance and continuous melting system. The model of the conventional fuel-fired melter is shown in Fig. 1. In the air-fuel-fired furnace, the heat transfer from above burner flame to glass melt is so low that the conventional melting technology is energy-intensive and time-consuming, especially in the melting and refining process. In addition, many emissions are generated due to the usage of fossil fuel, which brings more environmental pollution. Although many improvements have been performed in batching, heat transfer, melting, and refining, large energy consumption and high emissions are still the fatal problems in the conventional technology. With the rapid growth of glass usage and the increased energy and environment issues, it is crucial to develop a new glass-melting technology to solve these problems.

---

\*Paper based on a presentation at the 19<sup>th</sup> International Symposium on Plasma Chemistry (ISPC-19), 26–31 July 2009, Bochum, Germany. Other presentations are published in this issue, pp. 1189–1351.

‡Corresponding author

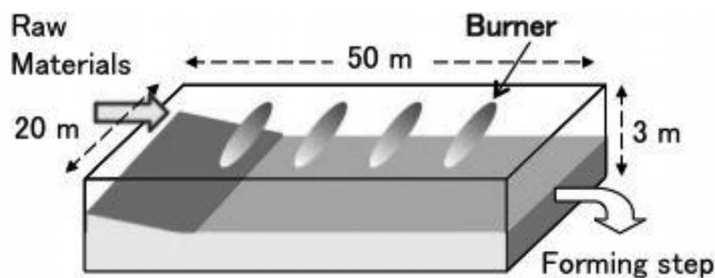


**Fig. 1** Conventional glass production.

Under the support of the New Energy and Industrial Technology Development Organization (NEDO) in Japan, an innovative in-flight glass-melting technology was developed [1–6]. The concept of the in-flight melting for glass production is illustrated in Fig. 2. The granulated raw material with small diameter is dispersed in thermal plasmas, and the powders contact fully with the plasma and burner flame. The high heat-transfer and temperatures of the plasma will melt the raw material quickly. In addition, the decomposed gas of carbonates is removed during the in-flight treatment to reduce the refining time considerably. Compared with the traditional glass production, the total vitrification time is evaluated only 2–3 h at the same productivity as the fuel-fired melter.

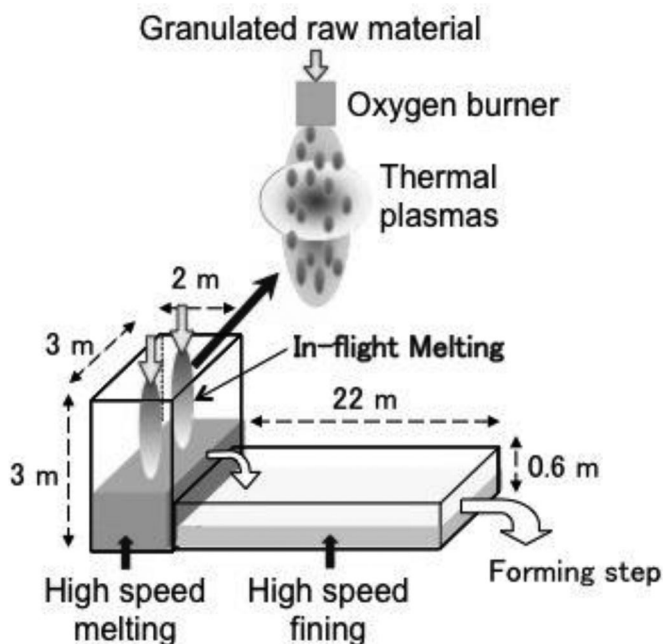


**Fig. 2** Innovative in-flight melting for glass production.

Thermal plasmas have been widely applied to many fields because of their unique advantages, such as high chemical reactivity, easy and rapid generation of high temperature, high enthalpy to enhance reaction kinetics, rapid quenching capability, and oxidation or reduction atmosphere in accordance with required chemical reaction. The usage of thermal plasmas in materials processing is becoming an increasingly active and attractive field for the development of new technology.

Among various thermal plasma reactors, arc plasma as an energy source with high energy efficiency has been applied in welding and cutting of metals, steelmaking, synthesis of nanoparticles, and spheroidization of metal particles. Most power sources for generating arc plasma are accomplished by using DC power supply, but it takes more cost in the apparatus for converting AC to DC [7,8]. The existing single- or three-phase AC power supplies have a characteristic of intermittent discharge which limits the application of arc plasma systems generated by the AC power supply. To obtain a more effective arc plasma reactor, a multiphase AC power supply was developed. Compared with other thermal plasmas, multiphase AC arc possesses the following advantages; high energy efficiency, large plasma volume, low velocity, easy scale-up, and low cost [9,10].

In this study, a stable 12-phase AC arc was generated by transformers at a commercial electric power system and the arc behavior was characterized by image analysis. Moreover, the effect of the flow rate of shield gas around the electrodes and the electrode configuration on the arc behavior and in-flight melting behavior of granulated glass raw material was investigated.

## MULTIPHASE AC ARC POWER SUPPLY

### Three- to twelve-phase conversion

A new type of arc reactor with multiphase AC discharge has been developed to obtain stable and continuous arc by transformers converting 3-phase AC to 6- or 12-phase AC. Figure 3 shows the electrical circuit diagram and temporary connection diagram of 12-phase AC arc reactor. The input of the 3-phase power supply was connected to commercial power lines. The primary coils of transformers are divided into two parts;  $\Delta$  connection and Y connection. The neutral points of the secondary coils in the transformers are connected to each other. The vector diagrams for converting 3-phase to multiphase are shown in Fig. 4. From Y connection, the voltage components  $V_x, V_y, V_z, V_x', V_y',$  and  $V_z'$  of the 6-phase AC are defined by the following equations:

$$V_i = V_m \sin(\omega t - n\pi/3), \quad (i = x, y, z; n = 0, 2, 4) \quad (1)$$

$$V_i' = V_m \sin(\omega t - n\pi/3), \quad (i = x, y, z; n = 3, 5, 7) \quad (2)$$

where  $V_m$  and  $\omega$  are the maximum value of the sinusoidal wave and the angular velocity, respectively. Here,  $\omega = 2\pi f$ ,  $f$  is the frequency of AC (50 Hz).

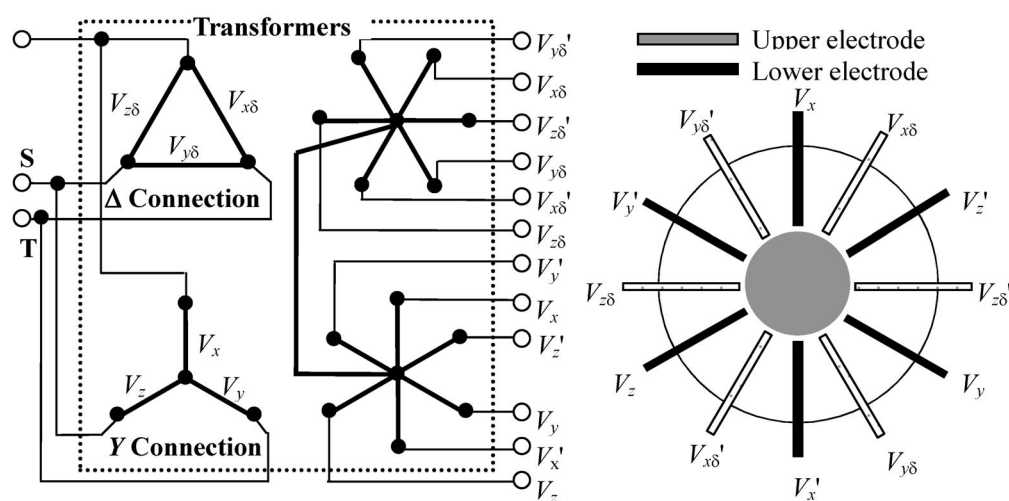
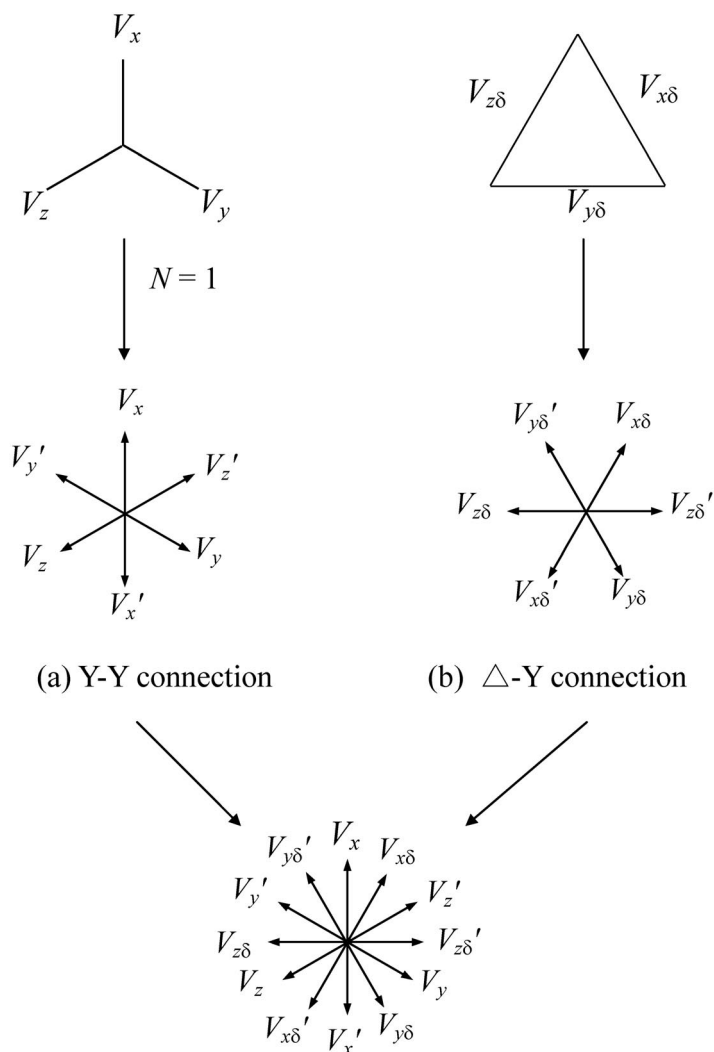


Fig. 3 Electrical circuit diagram and temporary connection diagram of 12-phase AC arc generation.



**Fig. 4** Vector diagrams for converting 3-phase to 12-phase.

From  $\Delta$  connection, the voltage components  $V_{x\delta}$ ,  $V_{y\delta}$ ,  $V_{z\delta}$ ,  $V_{x\delta}'$ ,  $V_{y\delta}'$ , and  $V_{z\delta}'$  of the 6-phase AC are defined as follows:

$$V_{i\delta} = V_m \sin(\omega t - n\pi/6), \quad (i = x, y, z; n = 1, 5, 9) \quad (3)$$

$$V_{i\delta}' = V_m \sin(\omega t - n\pi/6), \quad (i = x, y, z; n = 7, 11, 15) \quad (4)$$

The 6-phase power supply can be achieved by one vector described in Fig. 4a or b. The 12-phase power supply can be realized by the combination of two vectors (a) and (b).

The geometrical arrangement of electrode tips is illustrated in Fig. 5. When the distance between the electrodes Nos. 5 and 7 is treated as a unity, the distances among other electrode tips have the values as marked in Fig. 5. In general, the applied voltage between each electrode and the neutral point of the secondary coil of the transformer can be calculated by the following equation:

$$V_i = V_m \sin[\omega t - 2\pi(i - 1)/12], \quad (i = 1, 2 \dots 12) \quad (5)$$

From this equation, the differences of the voltage between the electrode No. 1 and the others are described as follows.

$$V_1 - V_2 = 2\sin(\pi/12)V_m \cos(\omega t - \pi/12) \quad (6)$$

$$V_1 - V_3 = V_m \cos(\omega t - \pi/6) \quad (7)$$

$$V_1 - V_4 = \sqrt{2}V_m \cos(\omega t - \pi/4) \quad (8)$$

$$V_1 - V_5 = \sqrt{3}V_m \cos(\omega t - \pi/3) \quad (9)$$

$$V_1 - V_6 = 2\cos(\pi/12)V_m \cos(\omega t - 5\pi/12) \quad (10)$$

$$V_1 - V_7 = 2V_m \cos(\omega t - \pi/2) \quad (11)$$

The electrode discharge is similar to the flat-plate gas discharge, therefore the electric field strength,  $E_{1-i}$ , between the electrode No. 1 and the others can be appropriately defined as follows:

$$E_{1-i} = (V_1 - V_i)/d_{1-i} \quad (12)$$

where  $d$  is the distance between two electrodes. Then, the following equations can be obtained:

$$E_{1-2} = V_m \cos(\omega t - \pi/12) \quad (13)$$

$$E_{1-3} = V_m \cos(\omega t - \pi/6) \quad (14)$$

$$E_{1-4} = V_m \cos(\omega t - \pi/4) \quad (15)$$

$$E_{1-5} = V_m \cos(\omega t - \pi/3) \quad (16)$$

$$E_{1-6} = V_m \cos(\omega t - 5\pi/12) \quad (17)$$

$$E_{1-7} = V_m \cos(\omega t - \pi/2) \quad (18)$$

From the above equations, it is noted that the ratio of the voltage amplitudes is equal to the ratio of the geometrical distances between the electrodes. As the phase shift is kept constant at every moment, the values of electric field strength among the electrodes are also constant at every moment.

For multiphase AC arc, the discharge behavior among the electrodes is complex, and the number of discharge path increases with the electrode number increasing. In the case of 3, 6, and 12-phase, the possible discharge paths are 3, 15, and 66, respectively.

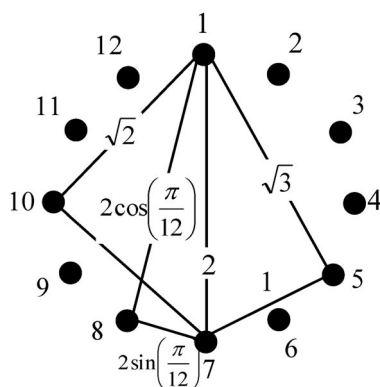


**Fig. 5** Geometrical arrangement of electrode tips for 12-phase.

### Power supply for multiphase AC discharge

To realize the power supply for the generation of 12-phase AC discharge, 12 sets of arc welding transformers with a single-phase AC (DAIHEN B-300, Japan) were used. These arc welding transformers are the conventional ones with the dropping characteristic. The input voltage, the maximum non-loading output voltage, the typical loading voltage, the power, and the output current are 200 V, 80 V, 35 V, 13.8 kW, and 300 A, respectively. Two pairs of six transformers are connected to the commercial AC line (3-phase 200 V, 50 Hz) with  $\Delta$  and Y connections. The output lines from transformers were connected directly to the corresponding electrodes of the reactor, as shown in Fig. 3.

## EXPERIMENTAL

### High-speed video observation

The schematic diagram of the experimental setup is shown in Fig. 6. It consisted of 12 electrodes, reaction chamber, powder feeder, and AC power supply. Twelve electrodes were symmetrically arranged by the angle of  $30^\circ$  and were divided into two layers, upper 6 electrodes and lower 6 electrodes. The electrode in diameter of 3.2 mm was tungsten (98 %) with thoria (2 %). City water was used to cool the electrode bodies and 99.99 % argon was injected around the electrodes to prevent them from oxidation at an appropriate flow rate. During a stable discharge, the diameter of arc was 100 mm and the distance between two layers of electrodes was 50 mm.

The discharge behavior of 12-phase arc with four kinds of electrode configuration were characterized by a high-speed video camera (HSV-500C<sup>3</sup>, NAC, Japan) installed on the top of the reactor as shown in Fig. 6. The arc discharge behavior was recorded at a speed of 500 fps (frames per second) and a shutter speed of 0.1 ms. It takes 20 ms for a periodic cycle while the frequency of power source used for 12-phase AC arc is 50 Hz. The phase transition time was 1.67 ms from one electrode to next one. A continuous video was recorded to observe the arc discharge behavior, then the captured video images were decomposed to individual images at an interval of 2 ms.

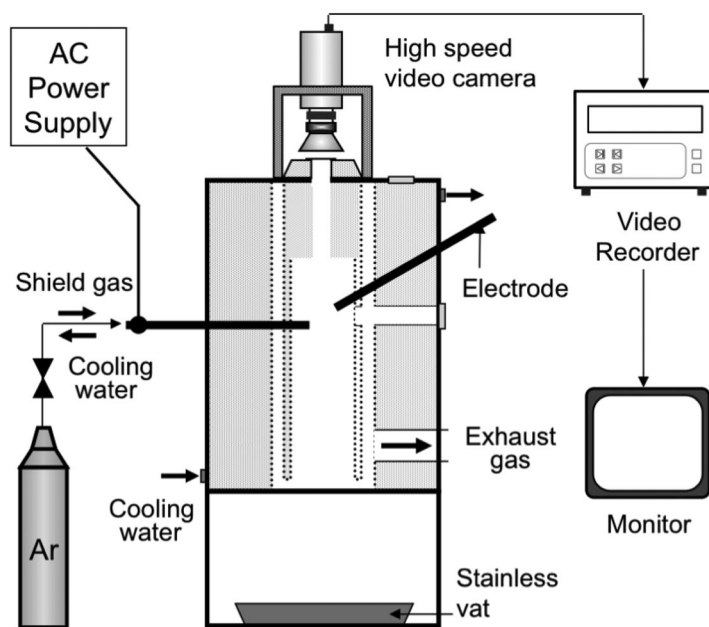


Fig. 6 Schematic diagram of experimental set-up of 12-phase AC arc.

## Particle in-flight melting

The experimental set-up was the same reactor described in Fig. 6, only replacement of a video camera with a water-cooling powder feeder nozzle. During the experiments, the input power was 50 kW. The discharge voltage and current of each electrode were 30–45 V and 80–130 A, respectively. The four kinds of arc configuration were used, which will be explained later, while the experiments of the in-flight melting were conducted by the electrode arrangement counterclockwise according to the phase sequence (normal discharge, configuration I). Two kinds of glass raw materials were used for the in-flight glass production: soda-lime glass and alkali-free glass. The powders treated by 12-phase arc were quenched on the stainless steel pan at a distance of 1050 mm below the nozzle.

Soda-lime glass is the most prevalent type of glass, used for windowpanes and glass containers for beverages, food, and some commodity items. The mixture of  $\text{SiO}_2$ ,  $\text{Na}_2\text{CO}_3$ , and  $\text{CaCO}_3$  was introduced to prepare the soda-lime glass with a target composition of 74 $\text{SiO}_2$ –16 $\text{Na}_2\text{O}$ –10 $\text{CaO}$  in mass %. To improve the fluidity of the powders in feeding and the melting efficiency, the raw materials was granulated into spherical powders by spray-drying method. The average diameter and porosity of granulated raw powders were 99  $\mu\text{m}$  and 73 %, respectively.

Alkali-free glass has received much attention owing to its excellent dielectric property, good rigidity, high intensity, and good thermal and chemical stability. It has been widely applied to many fields, such as liquid-crystal and electroluminescence displays, thin film transistors, charge-coupled devices, contact image sensors, solar cells, and glass fibers. The mixture of  $\text{SiO}_2$ ,  $\text{H}_3\text{BO}_3$ ,  $\text{Al}_2\text{O}_3$ ,  $\text{BaCO}_3$ , and  $\text{Sb}_2\text{O}_3$  was introduced to prepare the alkali-free glass with a target composition of 49 $\text{SiO}_2$ –15 $\text{B}_2\text{O}_3$ –10 $\text{Al}_2\text{O}_3$ –25 $\text{BaO}$ –1 $\text{Sb}_2\text{O}_3$  in mass %.

The structures of the melted powders were determined by X-ray diffractometry (XRD) on Miniflex (Rigaku, Japan) with  $\text{Cu } K_\alpha$  radiation at 30 kV and 15 mA. The data were collected in the  $2\theta$  range 3–90° with a step size of 0.02° and a scan speed of 4°  $\text{min}^{-1}$ . The vitrification degree is defined as the ratio of the reacted  $\text{SiO}_2$  in melted powders to total crystal  $\text{SiO}_2$  in raw material. The vitrification degree of raw material was quantitatively analyzed by the internal standard method [11]. First, the mixtures of pure  $\text{SiO}_2$  and ZnO (standard material) with various weights were used to obtain the calibration curve according to the peak intensities analyzed by XRD. Second, the mixture of the melted powders and ZnO was analyzed to estimate respective peak intensities. Finally, the reacted  $\text{SiO}_2$  can be accounted for the estimation of the vitrification degree, combining the ratio of  $\text{SiO}_2/\text{ZnO}$  peak intensity and the  $\text{SiO}_2$  content in the melted powders.

The morphology of the particles was observed by using a scanning electron microscope (SEM) apparatus (JSM5310, Jeol, Japan). The composition of the quenched powders was analyzed by inductively coupled plasma (ICP) spectroscopy on ICP-8100 (Shimadzu, Japan).

## RESULTS AND DISCUSSION

### In-flight melting characteristics of glass raw materials

Raw materials of the alkali-free glass powders with different flow rates of carrier gas were injected into the 12-phase AC arc at the flow rate of 30 g/min. The cross-section images of the particles were shown in Fig. 7 to observe the particle inside. The images indicate that the particle inside of the raw material has inhomogeneous structure, with many pores that were caused by the evaporation of water in slurry droplets when the particles were dried. However, the inside of the completely melted particles has a homogeneous and compact structure with spherical shape. The bubbles that appeared in the particle inside were formed by the decomposed gas from the raw material. Some incompletely melted particles with irregular shape, and the amount of unmelted particles increases with an increase of the carrier gas flow rate. The average diameter of the melted powders decreased at least 50 % of the original diameter. Similar results can be found from the electron probe microanalysis (EPMA) images of the melted alkali-free glass particles in Fig. 8. The particles fed by the carrier gas at 10 l/min have a smooth sur-

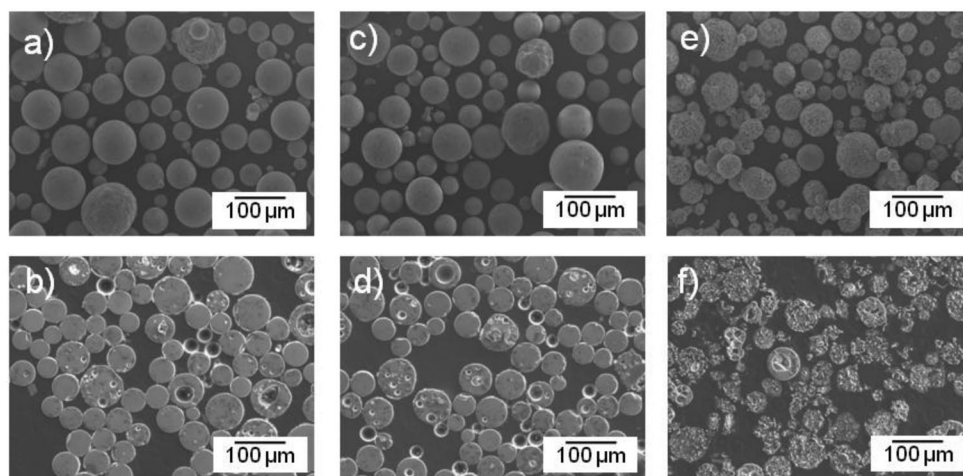


**Fig. 7** Alkali-free glass powders after in-flight melting by multiphase AC arc with different carrier gas flow rates; (a), (b): 10 l/min, (c), (d): 20 l/min, (e), (f): 30 l/min.

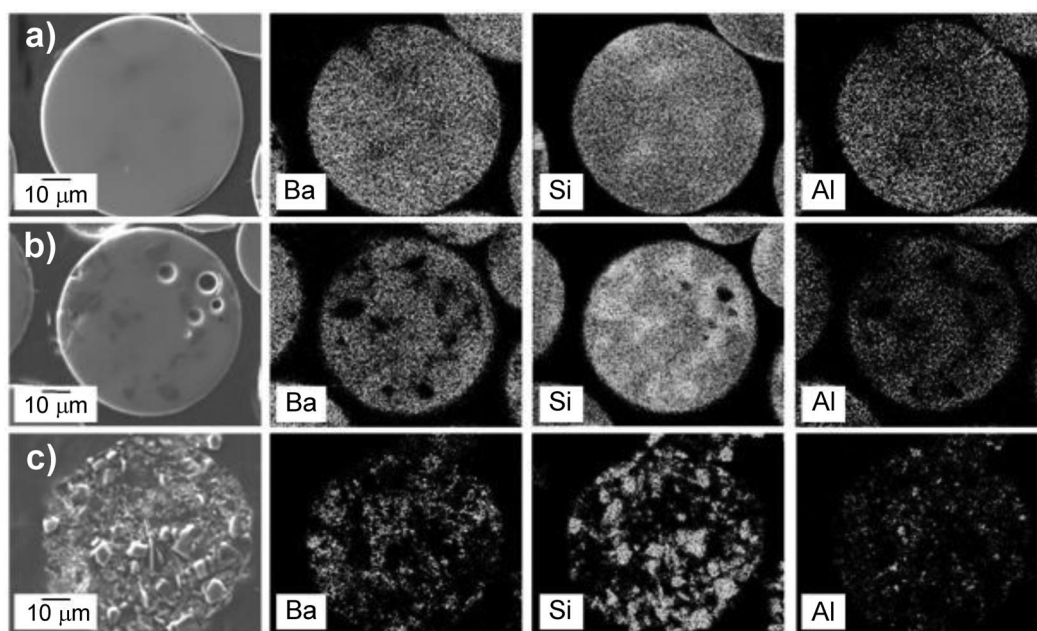


**Fig. 8** EPMA images of melted alkali-free glass particles by multiphase AC arc with different carrier gas flow rates; (a): 10 l/min, (b): 20 l/min, (c): 30 l/min.

face with spherical shape and less bubble. The melted particles at 10 l/min have homogeneous composition, although the particles at 20 and 30 l/min show the inhomogeneous composition.

Figure 9 shows the XRD patterns of the raw material of alkali-free glass and the powders treated by the 12-phase AC arc. The powders prepared at the flow rates of 10 and 20 l/min have only  $\text{SiO}_2$  peaks, but the powders prepared at 30 l/min still exhibits some  $\text{BaCO}_3$  peaks. It indicates that the  $\text{BaCO}_3$  and  $\text{H}_3\text{BO}_3$  in raw material completely decomposed at the smaller flow rate of carrier gas. During the plasma treatment, the main material  $\text{SiO}_2$  reacts with other compounds and converts into a

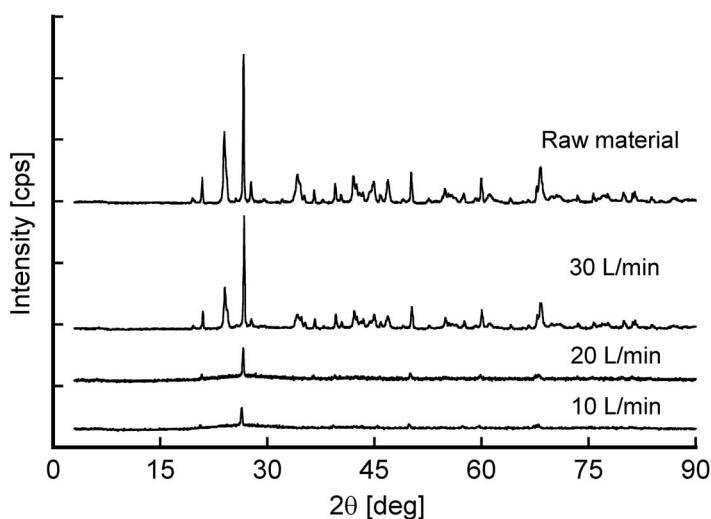


**Fig. 9** XRD patterns of melted alkali-free glass particles by multiphase AC arc with different carrier gas rates.

glass-like amorphous solid which is free of crystalline structure, the complicated process including many reactions is called vitrification. The intensity of  $\text{SiO}_2$  main peak (101) was decreased at the larger flow rate due to the reaction of crystal  $\text{SiO}_2$  with other compounds.

The XRD patterns of the soda-lime glass powders with different feed rates are shown in Fig. 10. The patterns show no obvious diffractive peaks of carbonates in the melted powders, indicating the decomposition of carbonates was completed in the flight melting process. Compared with the raw material, the intensity of  $\text{SiO}_2$  of the melted powders decreases, indicating the amorphous structure. The patterns without any peaks reveal that the reactions among compounds were completed during in-flight melting.

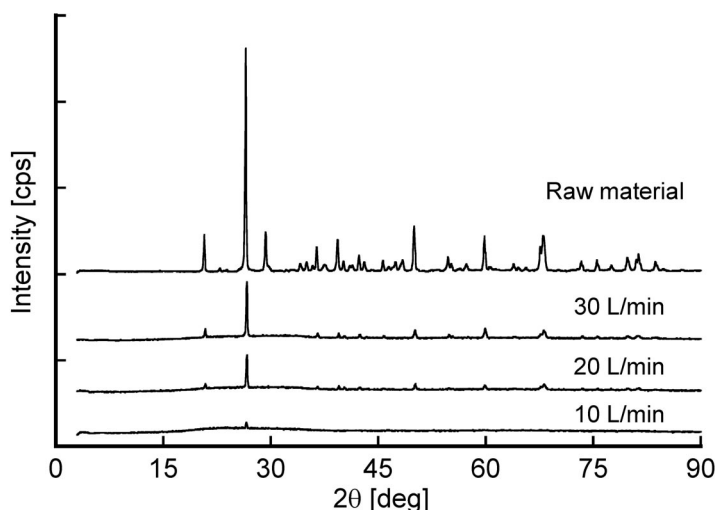


**Fig. 10** XRD patterns of melted soda-lime glass particles by multiphase AC arc with different carrier gas flow rates.

The vitrification degree of the powders is shown in Fig. 11 for the alkali-free and the soda-lime glass powders. The analytical results show that the highest vitrification degree was obtained at the carrier gas flow rate of 10 l/min, but the vitrification degree decreases at 30 l/min especially for the alkali-free glass powders. There are two main reasons to explain the low degree of vitrification at larger flow rate of the carrier gas. Larger flow rate leads to lower plasma temperature as well as to shorter residence of the powders, then less energy was transferred to the powders during the flight in the plasma. The degree of vitrification of the alkali-free glass is lower than that of the soda-lime glass due to higher viscosity of the alkali-free glass, resulting in slower vitrification. The reaction and melting start from the surface of the particle, then propagate into the inside. The higher viscosity of molten glass on the surface will delay the melting and the removal of decomposed gas inside the particle in the case of the alkali-free glass.

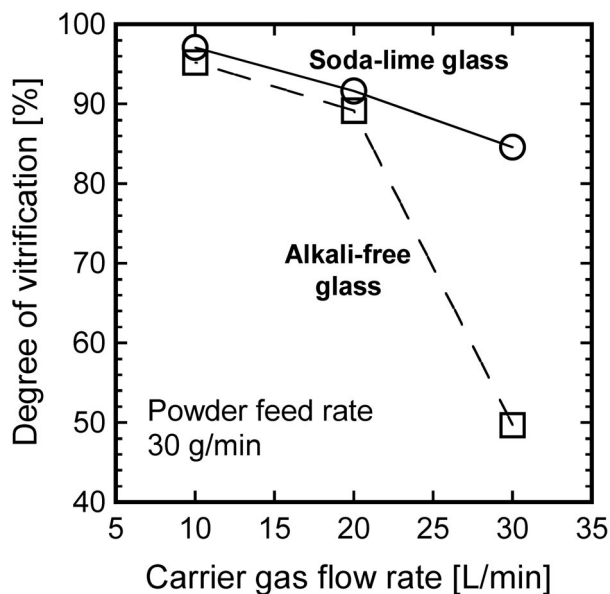


**Fig. 11** Effect of carrier gas flow rate on the degree of vitrification of the melted powders by multiphase AC arc.

Disodium oxide ( $\text{Na}_2\text{O}$ ) in the soda-lime glass and  $\text{B}_2\text{O}_3$  in the alkali-free glass are the indispensable materials to change the properties of glasses, introduced from the reagents of  $\text{Na}_2\text{CO}_3$  and  $\text{H}_3\text{BO}_3$ , respectively. The main function of  $\text{Na}_2\text{O}$  and  $\text{B}_2\text{O}_3$  is to reduce the viscosity and softening temperature of each glass by controlling their content. The variations of content of  $\text{Na}_2\text{O}$  in soda-lime glass powders and  $\text{B}_2\text{O}_3$  in alkali-free glass powders are shown in Figs. 12 and 13, respectively, as a function of the carrier gas flow rate. With the flow rate of carrier gas increasing, the evaporation rate of  $\text{Na}_2\text{O}$  and  $\text{B}_2\text{O}_3$  in the melted powders decreases, which indicates the temperature of the powders in the plasma was lower.

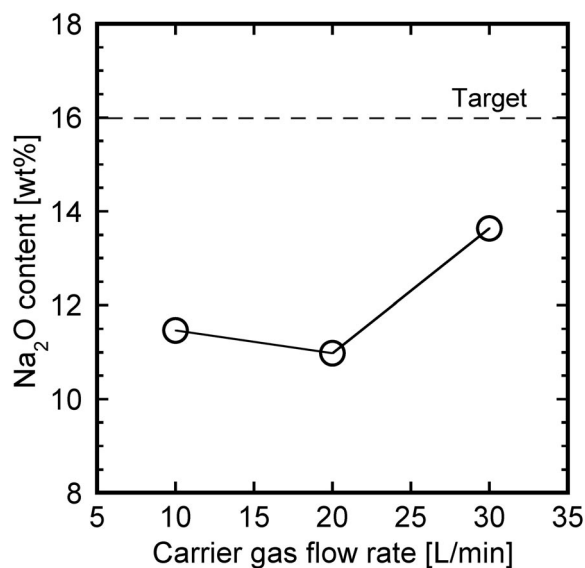


Fig. 12 Effect of carrier gas flow rate on Na<sub>2</sub>O content of melted soda-lime glass particles by multiphase AC arc.

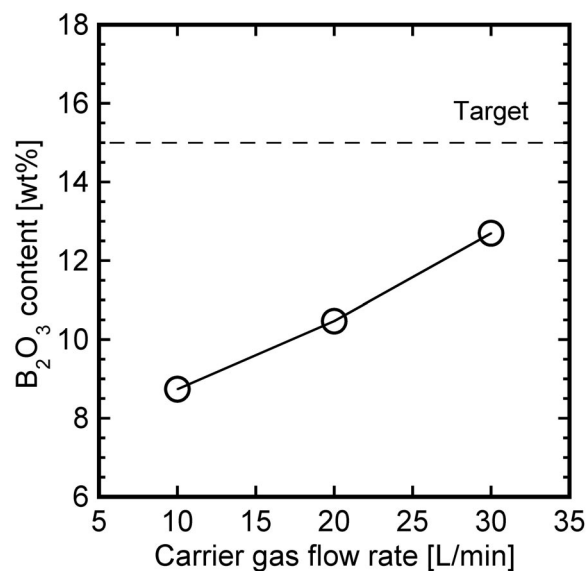
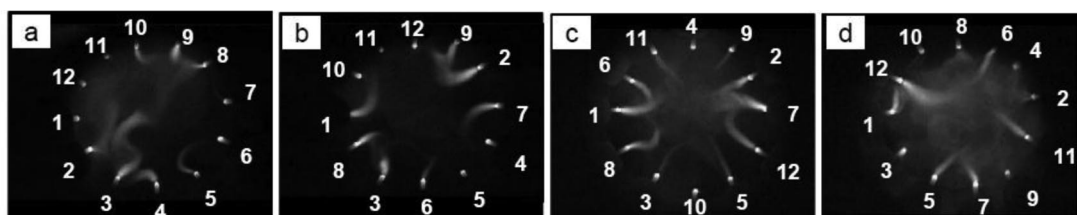


Fig. 13 Effect of carrier gas flow rate on B<sub>2</sub>O<sub>3</sub> content of melted alkali-free glass particles by multiphase AC arc.

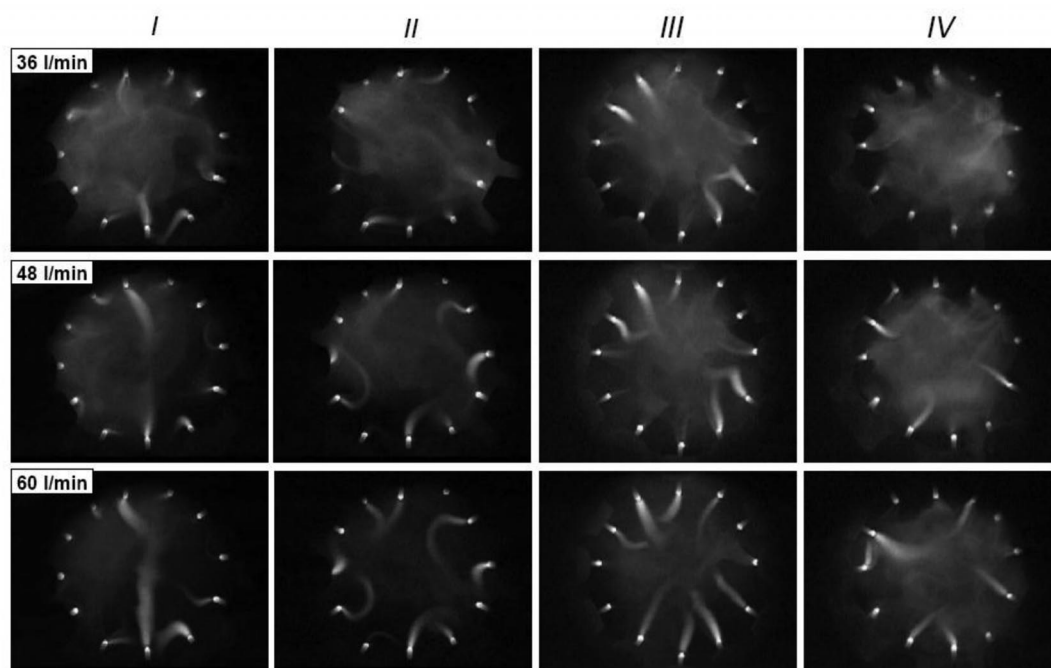
### Arc discharge behavior with different electrode configurations

Figure 14 illustrates four kinds of electrode configuration for generating the 12-phase arc. The number marked on the figure indicates the phase-shifting order. All the electrodes are arranged counterclockwise according to the phase sequence in configuration I (normal discharge). In configuration II, the upper 6 electrodes keep fixed and 6 lower electrodes rotate 180° clockwise. In configuration III, the lower electrodes are arranged counterclockwise by comparison with configuration II. Interval phases are connected counterclockwise by odd and even order in configuration IV.



**Fig. 14** Electrode configurations of 12-phase AC arc: (a) configuration I, (b) configuration II, (c) configuration III, (d) configuration IV.

The discharge behavior is displayed in Fig. 15 for four configurations, indicating a complete discharge cycle at an interval of 20 ms. Among all electrode configurations, the main discharge generates between Nos. 1–7, 2–8, 3–9, 4–10, 5–11, and 6–12. The maximum phase difference exists between the opposite electrodes except configuration IV. Configurations I, III, and IV display the rotating and regular discharge behavior in the counterclockwise direction. The stronger arc generation concentrates at the center in the cases of configurations I and III, indicating higher plasma temperature at the arc center. Compared with configuration I, configuration III has a couple of strong and short arcs. The arc discharge almost takes place between close electrodes in the case of configuration II. For configuration IV, the arc discharge mainly occurs between two electrode intervals, which provide a large plasma region. Observing the discharge photos, the arc luminance area is changed with the different electrode configurations. The luminance area of the arc in configuration II looks smallest, and largest in configuration IV. The different plasma shapes indicate the diverse discharge path and arc temperature for each configuration. The high-temperature region can be controlled according to the processing requirements by different electrode configurations.



**Fig. 15** Arc discharge behavior of 12-phase AC arc at different flow rates of argon sheath gas for configurations I, II, III, and IV.

Figure 15 also shows the arc discharge behavior at different total flow rates of sheath gas. As the flow rate of sheath gas increases, the luminance area becomes smaller and the plasma flame becomes narrower and longer. The flow rate of sheath gas prolongs the plasma flame and makes the plasma flame close to the arc center. This improves the plasma temperature at the center of arc.

In this study, the captured image was transformed into binary image by setting luminance value at 50 to estimate the luminance area according to pixel scale, then the ratio of luminance area is defined as the luminance area divided by the whole area. Figure 16 shows the fluctuation of the luminance area ratio as a function of discharge time under different flow rates of sheath gas. The luminance area ratio is obvious to decrease with the increased flow rate of sheath gas in configurations I, II, and III. The luminance areas in configurations III and IV look larger than that in configurations I and II. The calculated results are in agreement with above discharge images. Moreover, the long residence time and broad flame of plasma lead to a flat fluctuation of the luminance area ratio at small flow rate of sheath gas. The variation of the luminance area ratio in configuration IV is smaller with the changed flow rate of sheath gas due to its diffuse discharge characteristic.

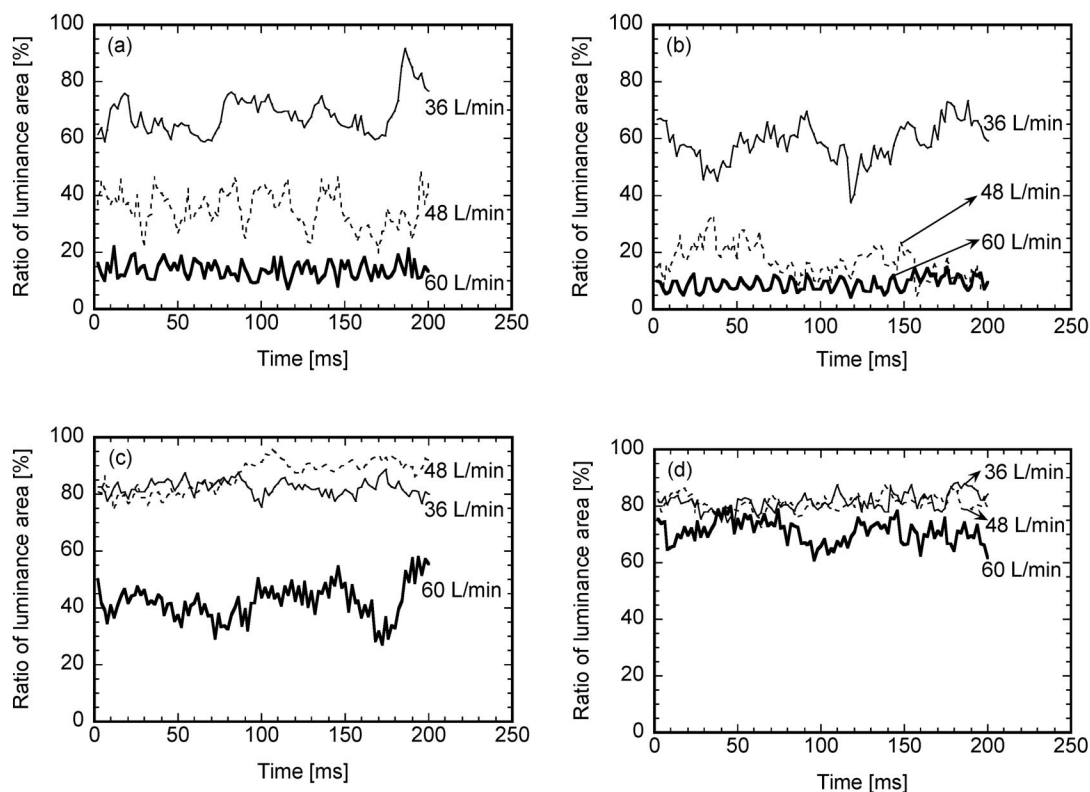


**Fig. 16** Fluctuation of ratio of luminance area of 12-phase AC arc at different flow rates of sheath gas: (a) configuration I, (b) configuration II, (c) configuration III, (d) configuration IV.

Figure 17 shows the variation of vitrification of powders treated at different total flow rates of sheath gas. The granulated glass raw materials were injected into the plasma at the feed rate of 30 g/min with air carrier gas of 20 l/min. The vitrification degree is higher at larger flow rate of sheath gas. Although larger flow rate of sheath gas results in stronger cooling effect on the arc edge, longer plasma flame leads to the higher temperature at the arc center. Since the diameter of nozzle is 4 mm, which is

relatively smaller than the arc diameter, most granulated particles pass through the central region of the arc. Hence, higher temperature at the arc center causes higher vitrification degree. The characteristic of configuration III with a couple of stronger discharge results in the smaller change in vitrification degree. The special discharge between near electrodes in configuration II brings about lower center temperature, which explains its lower vitrification degree.

Comparing the variation of arc discharge behavior in Fig. 15 and the vitrification degree of glass raw material in Fig. 17, configuration I shows the highest vitrification degree, but not highest average ratio of the luminance area. Similarly, configuration IV has the highest average ratio, but a little lower vitrification degree. There is no invariable relationship between the area ratio of luminance and the vitrification degree of glass raw material. The average ratio of luminance area only indicates the degree of plasma uniformity, and it cannot reflect the real temperature of the plasma. The vitrification of raw material mostly depends on the center plasma temperature. The real temperature distribution will be measured by enthalpy probe in the coming future.

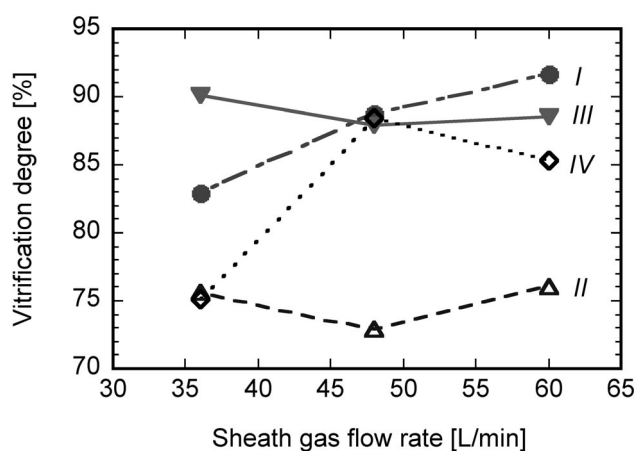


**Fig. 17** Vitrification degree of soda-lime glass powders at different flow rates of sheath gas with different arc configurations of 12-phase AC arc.

## CONCLUSIONS

The multiphase AC arc possesses the following advantages for material synthesis and processing; high energy efficiency, large plasma volume, low velocity, easy scale-up, and low cost. The present study reveals that the electrode configuration and the sheath gas have strong effects on the arc and melting behavior. The diffuse discharge behavior in configuration IV shows the highest luminance area and the uniform distribution of plasma. The control of high-temperature region can be achieved by adjusting electrode configuration. With the flow rate of sheath gas increasing, the average ratio of luminance area decreases and the vitrification degree increases. The characterized arc discharge behavior explains the in-flight melting behavior of granulated raw particles very well.

## ACKNOWLEDGMENTS

The financial support provided by Energy Innovation Program of NEDO (New Energy and Industrial Technology Development Organization) is gratefully acknowledged.

## REFERENCES

1. Y. Yao, T. Watanabe, T. Yano, T. Iseda, O. Sakamoto, M. Iwamoto, S. Inoue. *Sci. Technol. Adv. Mater.* **9**, 025013 (2008).
2. Y. Yao, M. M. Hossain, T. Watanabe, F. Funabiki, T. Yano. *Chem. Eng. J.* **139**, 390 (2008).
3. Y. Yao, M. M. Hossain, T. Watanabe, T. Tsujimura, F. Funabiki, T. Yano. *Thin Solid Films* **516**, 6622 (2008).
4. Y. Yao, K. Yatsuda, T. Watanabe, F. Funabiki, T. Yano. *Chem. Eng. J.* **144**, 317 (2008).
5. F. Funabiki, T. Yano, Y. Yao, T. Watanabe. *J. Am. Ceram. Soc.* **91**, 3908 (2008).
6. M. M. Hossain, Y. Yao, T. Watanabe, F. Funabiki, T. Yano. *Chem. Eng. J.* **150**, 561 (2009).
7. J. E. Harry, R. Knight. *J. Phys. D: Appl. Phys.* **17**, 343 (1983).
8. J. E. Harry, R. Knight. *IEEE Trans. Plasma Sci.* **9**, 248 (1981).
9. K. Matsumoto. *Plasma Sources Sci. Technol.* **5**, 245 (1996).
10. T. Matsuura, K. Taniguchi, T. Watanabe. *Thin Solid Films* **515**, 4240 (2006).
11. D. E. Willis. *Chromatographia* **5**, 42 (1972).